Electrochimica Acta 260 (2018) 168–176

Contents lists available at ScienceDirect

Electrochimica Acta

journal homepage: www.elsevier.com/locate/electacta

Peptide templated AuPt alloyed nanoparticles as highly efficient bi-functional electrocatalysts for both oxygen reduction reaction and hydrogen evolution reaction

Wen Wu [a], Zhenghua Tang [a, b, *], Kai Wang [a], Zhen Liu [c], Ligui Li [a, b], Shaowei Chen [a, d]

[a] Guangzhou Key Laboratory for Surface Chemistry of Energy Materials, New Energy Research Institute, School of Environment and Energy, South China University of Technology, Guangzhou Higher Education Mega Centre, Guangzhou, 510006, China
[b] Guangdong Provincial Key Laboratory of Atmospheric Environment and Pollution Control, Guangdong Provincial Engineering and Technology Research Center for Environmental Risk Prevention and Emergency Disposal, School of Environment and Energy, South China University of Technology, Guangzhou Higher Education Mega Centre, Guangzhou, 510006, China
[c] Department of Physics & Engineering, Frostburg State University, Frostburg, MD 21532-2303, United States
[d] Department of Chemistry and Biochemistry, University of California, 1156 High Street, Santa Cruz, CA 95064, United States

ARTICLE INFO

Article history:
Received 7 September 2017
Received in revised form
19 October 2017
Accepted 10 November 2017
Available online 11 November 2017

Keywords:
Peptide Z1
AuPt alloys
Bi-functional electrocatalysts
Oxygen reduction reaction
Hydrogen evolution reaction

ABSTRACT

Peptide driven metallic nanomaterials fabrication under mild conditions has become a significant research thrust recently, thanks to its capability to generate multifunctional materials with tunable electronic and catalytic properties. Herein, peptide Z1 is employed to fabricate a series of AuPt alloyed nanoparticles with different Au-to-Pt ratios. The morphology is examined by electron microscopic techniques, and well-defined peanut-shape is observed for $Au_{33}Pt_{67}$ while spherical particles are obtained for the other samples. The AuPt alloys demonstrate effective electrocatalytic activity toward both oxygen reduction reaction (ORR) and hydrogen evolution reaction (HER) and $Au_{33}Pt_{67}$ exhibits the best bifunctional electrocatalytic performance. Its ORR activity is superior than commercial Pt/C in alkaline media, verified by the positive onset potential (+1.02 V vs. RHE) and large diffusion-limited current density, while its HER activity is comparable with Pt/C, evidenced by the small overpotential at 10 mA cm^{-2} (−171 mV vs. RHE) and low Tafel slope. Moreover, $Au_{33}Pt_{67}$ exhibits markedly higher long-term durability than Pt/C for both ORR and HER. The excellent activity and stability for ORR and HER are ascribed to Au alloying Pt induced synergistic effects. The results highlight the advantages of using peptide to fabricate bi-functional or multiple functional electrocatalysts with desirable activity and robust stability.

1. Introduction

Bimetallic nanoparticles have been continuously gaining increasing research attentions as catalysts and electrocatalysts, mainly thanks to their distinct physical and chemical properties (optical, electronic, magnetic, and so on) as well as the alloying effects [1–3]. Compared with their counterparts monometallic nanoparticles, the synergistic effects during the catalytic process from the bimetallic nanoparticles have empowered them enhanced catalytic activities [4]. Note that, the catalytic properties of the catalyst are highly dependent on their surface structure, and the introduction of another metallic component can significantly modify the size, shape/morphology and surface composition of the catalyst, which could further facilitate fine-tuning of their catalytic performance. For instance, PtM (M=Fe, Co, Ni, Pd, Au etc.) alloys have demonstrated superior catalytic activity than Pt nanoparticles as electrocatalysts toward ORR and HER [5–7]. It is worth noting that, ORR is a key electrochemical process which determines the energy conversion efficiency of fuel cells and metal-air batteries [8–10], while HER is critically important for the production of clean and sustainable energy [11,12].

Among a series of metals to alloy Pt, Au is of particular interest to us in terms of its inertness in the bulk state and high catalytic activity at the nanoscale [13–15]. Previously, AuPt nanostructures

* Corresponding author. Guangzhou Key Laboratory for Surface Chemistry of Energy Materials, New Energy Research Institute, School of Environment and Energy, South China University of Technology, Guangzhou Higher Education Mega Centre, Guangzhou, 510006, China.
E-mail address: zhht@scut.edu.cn (Z. Tang).

https://doi.org/10.1016/j.electacta.2017.11.057
0013-4686/

have already been proved and served as perfect synergistic platforms for catalyzing either ORR or HER or both reactions. Luo et al. examined the catalytic activity and bimetallic composition of carbon supported gold platinum nanoparticles toward ORR, and found the maximized mass activity was achieved with the sample of 60–80% Au [16]. In 2010, Han group reported the synthesis of bimetallic hetero-nanostructure consisting of a dendritic Pt shell and structured Au core by seed growth method, and higher activity and durability than Pt nanoparticles toward ORR were achieved [17]. Moreover, Au–Pt alloyed nanowire networks [18], AuPt alloyed flower-like assembly nanochains [19], Pt–Au superlattice arrays [20], porous AuPt nanoparticles [21] and other AuPt nanostructures have been recorded to possess enhanced ORR activity and stability. In addition, Shao et al. reported the direct synthesis of core-shell AuPt@Pt nanocrystals supported on reduced graphene oxide (RGO) which exhibited enhanced electrocatalytic performance toward HER [22], while such excellent HER activity can also be obtained from RGO supported bimetallic AuPt nanodendrites by Wang and co-workers [23]. Recently, Feng et al. developed an ultrasonication-assisted wet-chemical fabrication of uniform AuPt nanodendrites, and the as-prepared architecture displayed remarkable catalytic performance toward both ORR and HER than commercial Pt black and Pt/C [24].

Since the catalytic performance is closely associated to the surface structure/composition of the catalyst, to achieve better performance, precise control or subtle modification of the surface structure/composition has arisen as the grandest challenge for bimetallic nanoparticles as electrocatalysts. To fabricate alloyed nanoparticles with well-defined structures, organic molecules [2], dendrimer [25], biomolecules including protein [26], DNA [27] especially peptide [28,29] have all been extensively and intensively employed as ligand/template to tune/control the surface structure. Peptide-based approach exploits such a new avenue for fabricating multifunctional nanomaterials under mild conditions based on the following rationales: First of all, the preparation process was normally conducted in water without using organic solvents at room temperature, almost zero-energy input, and more importantly, environmentally friendly; Secondly and more significantly, these peptide sequences hold specific binding affinities for target metal substrates, and they can direct the nuclei growth and nanoparticle formation hence precisely control the size, shape/morphology, composition as well as subtle surface structure of the metal nanomaterials [26,28,30]. Bedford et al. successfully examined the nanoscale surface segregation of AuPd bimetallic nanoparticles, and surface-dependent catalytic activities were achieved for methanol oxidation reaction [31]. Kim group reported the fabrication and catalytic response to ORR of surface-composition-controlled AuPt bimetallic nanoparticles on carbon nanotubes [32]. Recently and notably, our group also successfully demonstrated the facile fabrication of peptide A4 based AuAg alloyed nanoparticle networks [33] and FlgA3 templated AuPd bimetallic spherical nanoparticles [34], and both bimetallic systems exhibited excellent electrocatalytic activity toward ORR.

Herein, we report a facile fabrication of Z1 templated AuPt bimetallic nanoparticles and their electrocatalytic performance for both ORR and HER. Peptide Z1, with a sequence of KHKHWHW, has been found as a multi-material binder to Au, ZnS and CdS by using a yeast surface display system by Belcher group in 2005 [35]. In 2013, Knecht group quantified the binding affinity (Gibbs free energy ΔG) of Z1 to Au surface through quartz crystal microbalance [36], and Z1 templated Au nanoparticles also demonstrated effective catalytic activity toward 4-nitrophenol reduction [37]. In this study, peptide Z1 was employed as a template to stabilize the AuPt alloyed nanoparticles with different Au-to-Pt ratios through a facile wet chemical approach. Electron microscopic studies revealed the well-defined peanut shape of the $Au_{33}Pt_{67}$ sample, while spherical particles were observed for the other samples in the series. The as-prepared alloys exhibited effective activity toward both ORR and HER. The $Au_{33}Pt_{67}$ sample showed the best bi-functional activities in alkaline electrolyte with ORR performance superior than Pt/C and HER activity close to Pt/C. Intriguingly, the long-term stability of the $Au_{33}Pt_{67}$ sample was drastically higher than that of Pt/C in both ORR and HER performances.

2. Materials and methods

2.1. Chemicals

Peptide Z1 (KHKHWHW, >95%, Top-Peptide, Shanghai, China), Hydrogen tetrachloroauric acid (III) trihydrate ($HAuCl_4 \cdot 3H_2O$, 98%, Energy Chemicals, Shanghai, China), Chloroplatinic acid hexahydrate ($H_2PtCl_6 \cdot 6H_2O$, 99%, Energy Chemicals, Shanghai, China), Sodium borohydride ($NaBH_4$, 98%, Aladdin Industrial Corporation, Shanghai, China), Nafion (5 wt%, Alfa Aesar) and Pt/C (20 wt %, Alfa Aesar). All chemicals were used as received without further purification, and ultrapure water (18.2 MΩ cm) was employed in all experiments.

2.2. Synthesis of Z1 templated AuPt nanoparticles

The AuPt alloyed nanoparticles have been fabricated by a modified procedure in our previous reports [33,34,38]. For all the samples, the metal-to-peptide ratio was kept as 30: 1, while the Au-to-Pt ratios were set as 100: 0, 83: 17, 67: 33, 50: 50, 33: 67, 17: 83 and 0: 100. The $Au_{33}Pt_{67}$ sample was prepared as follows. Briefly, 200 μL Z1 aqueous solution (1 mM) was diluted into 1.53 mL H_2O, followed by the addition of a mixture of 50 μL $HAuCl_4$ (40 mM) and 100 μL H_2PtCl_6 (40 mM) aqueous solution under slight agitation. The mixture was incubated for 20 min. Then 120 μL freshly prepared $NaBH_4$ (0.1 M) aqueous solution was added rapidly, and the solution turned from yellow to black immediately. The solution was kept stirring at least 1 h at ambient temperature. The other samples were synthesized in a similar manner by changing the volume of the $HAuCl_4$ and H_2PtCl_6 solutions correspondingly.

2.3. Characterizations

The crystal structure of the samples was measured by X-ray diffraction (XRD) using a Bruker D8 diffractometer with Cu K_α radiation ($\lambda = 0.1541$ nm). The composition and valence state of the nanoparticles were analyzed by X-ray photoelectron spectroscopy (XPS) with an Escalab 250 photoelectron spectrometer (Thermo Fisher Scientific, USA). The UV–visible absorbance test was carried out on a Shimadzu 2600/2700 UV–visible scanning spectrophotometer with a 1 cm quartz cuvette. The size and morphology of the samples were characterized by a high-resolution transmission electron microscope (JEOL TEM-2010) coupled with an energy dispersive X-ray spectroscopy (EDS) system. The subtle surface microstructure of the $Au_{33}Pt_{67}$ sample was examined by a high angle annular dark-field (HAADF) scanning transmission electron microscope (STEM) at an acceleration voltage of 200 kV. The elemental distribution in the $Au_{33}Pt_{67}$ sample was observed by energy dispersive X-ray spectroscopy (EDS) mapping.

2.4. Electrochemical measurements

The ORR measurements were conducted on a CHI 750E electrochemical workstation (CH Instruments Inc.) in both 0.1 M KOH and 0.1 M $HClO_4$ aqueous solution at room temperature with a three-electrode system. The system including a glassy carbon-disk

electrode (diameter 5 mm, geometrical area of 0.196 cm^2, Pine Instrument Inc., RRDE collection efficiency is 37%) as the working electrode, a AgCl/Ag electrode in 0.1 M KOH and a saturated calomel electrode (SCE) in 0.1 M $HClO_4$ as the reference electrode and a platinum wire as the counter electrode. An appropriate amount of catalyst aqueous solution containing 20 μg solute was dropwise cast onto the glassy carbon disk after cleaned by polishing with aqueous slurries of 0.2 μm alumina powders on a polishing microcloth, and dried at room temperature. For commercial Pt/C (20 wt %), 2 mg Pt/C was well-dispersed in 1 mL ethanol and 10 μL of the ink was cast onto the glassy carbon disk electrode and dried at ambient temperature. Subsequently, 10 μL diluted Nafion solution (20 μL Nafion in 1 mL ethanol) was dropped on the dried samples and Pt/C catalyst. Cyclic voltammetric (CV) curves and linear sweep voltammograms (LSV) with various rotation rates from 100 to 2500 rpm were acquired at a scan rate of 10 mV s^{-1} in oxygen-saturated 0.1 M KOH and 0.1 M $HClO_4$ solution. The RRDE voltammetric measurements were conducted at the potential ranged from −0.03 V to +1.17 V and the ring potential was set as +0.5 V. The stability of the catalysts was tested by chronoamperometric measurements at +0.5 V with a rotation rate of 900 rpm and accelerated durability tests (ADT) from +0.6 V to + 1.0 V at 50 mV s^{-1} was conducted in O_2-saturated 0.1 M KOH solution before and after 2, 500 cycles of potential scans.

The HER measurements were performed on a CHI 750E electrochemical workstation (CH Instruments Inc.) in both 0.1 M KOH and 0.5 M H_2SO_4 aqueous solutions with scan rate of 10 mV s^{-1} at ambient temperature. In both solutions, a glassy carbon electrode (geometrical area of 0.07 cm^2) and a graphite rod was employed as the working electrode and the counter electrode, respectively. In 0.1 M KOH, a AgCl/Ag electrode was employed as the reference electrode, while a SCE was used as reference electrode in 0.5 M H_2SO_4. 1.25 times amount of sample and Pt/C catalysts used in ORR test was cast onto the working electrode in HER. The durability of the $Au_{33}Pt_{67}$ catalysts was assessed by accelerated linear potential sweeps conducted repeatedly on the electrode at a scan rate of 100 mV s^{-1}.

In all electrochemical tests, the potential was referenced to a Reversible Hydrogen Electrode (RHE): $E_{(RHE)} = E_{(Ag/AgCl)} + (0.197 + 0.0591\ pH)$ V, $E_{(RHE)} = E_{(SCE)} + (0.24 + 0.0591\ pH)$ V.

3. Results and discussions

3.1. Electron microscopic image analysis of AuPt bimetallic nanoparticles

Fig. S1 presents the UV–visible absorbance spectra of the peptide Z1 templated AuPt nanoparticles before and after the reduction by $NaBH_4$. Prior to the reduction, there are two absorbance peaks located at ~210 nm and ~260 nm, which can be attributed to the ligand-to-metal charge transfer to Au and Pt surface [39,40], respectively. Upon the reduction of $NaBH_4$, the absorbance arising from peptide coordinated Au^{3+} and Pt^{2+} no longer exist, and the featureless absorbance profile with abroad absorption was noted for each material, indicating the formation of nanomaterial [41].

The samples were then examined by electron microscopic techniques. The representative TEM and HR-TEM image of the $Au_{33}Pt_{67}$ sample were shown in Fig. 1a and b. Peanut shape was observed for the $Au_{33}Pt_{67}$ sample, and some peanuts connect with each other. Such peanut morphology can be more readily identified in HAADF-STEM image inset in Fig. 1c and Black field-TEM in Fig. 1d. Continuous lattice fringes can be easily recognized in the HR-TEM image (Fig. 1b), and the d-spacing of the adjacent fringe is 0.232 nm. Note that, this spacing value is in the between of pure Au (0.234 nm, JCPDS-04-0784) and pure Pt (0.227 nm, JCPDS-04-0802), indicating the formation of AuPt alloyed structure. From the HR-TEM image of a single $Au_{33}Pt_{67}$ particle, the cross-sectional line-scan profile was conducted. As shown in Fig. 1c, the Au element hold almost identical distribution trend with the Pt element, further manifesting the AuPt alloy formation. To closely examine the Au and Pt elemental distribution of the $Au_{33}Pt_{67}$ sample, elemental energy dispersive X-ray spectroscopic (EDS) mapping was conducted and presented in Fig. 1e–g. It can be noted that, both the Au and Pt species were homogenously distributed and exhibited random elemental inter-mixing. The uniform Au–Pt overlapping pattern further confirms that homogeneous AuPt alloys were obtained.

The typical TEM images of the $Au_{83}Pt_{17}$, $Au_{67}Pt_{33}$, $Au_{50}Pt_{50}$, $Au_{17}Pt_{83}$, and Pt_{100} samples can be found in Fig. S2. For the Pt_{100} sample, bulky aggregates cluster together, while for the $Au_{17}Pt_{83}$ sample, slight aggregation can also be observed. Besides that, well-defined spherical nanoparticles can be easily identified for the other samples, and the average diameter was calculated as 4.05 ± 0.56 nm, 3.46 ± 1.13 nm, 3.45 ± 0.59 nm, 3.72 ± 0.81 nm and 31.66 ± 8.94 nm for $Au_{83}Pt_{17}$, $Au_{67}Pt_{33}$, $Au_{50}Pt_{50}$, $Au_{17}Pt_{83}$, and Pt_{100} (Table S1), respectively.

3.2. XRD and XPS analysis

The structure of the Au_{100}, $Au_{33}Pt_{67}$, Pt_{100} samples was then studied by X-ray diffraction (XRD) measurements. From Fig. 2a, it can be seen that, there are four well-defined peaks located at 2θ = 39.06, 45.39, 66.31, and 80.21, which can be assigned to the (111), (200), (220), and (311) planes of the fcc alloyed structure. In addition, the diffraction peaks are located between the Au_{100} sample (JCPD-04-0784) and the Pt_{100} sample (JCPD-04-0802) [20], further implying the alloyed structure was successfully obtained.

The composition and valence state of the series was probed by X-ray photoelectron spectroscopy (XPS). Fig. S3 shows the survey scan spectra of the Au_{100}, $Au_{33}Pt_{67}$ and Pt_{100} samples. From XPS, the Au-to-Pt ratio can be estimated as 30.2: 69.8 for the $Au_{33}Pt_{67}$ sample, which approximately agrees with the initial loading ratio (1: 2). The core-level XPS spectra of the Au4f and Pt4f electrons can be found in Fig. 2b and c. For the Pt4f electrons, the binding energies at ~71.3 eV and ~74.7 eV are attributed to $Pt4f_{7/2}$ and $Pt4f_{5/2}$ electrons, and both peaks can be de-convoluted into doublet peaks as well. The strong doublets at the binding energies of 71.1 eV and 74.4 eV are assigned from metallic Pt, while the other doublets at the binding energies of 72.3 eV and 76.1 eV are attributed to Pt(II). Based on the integrated area from the $Pt4f_{7/2}$ electrons, the percentage of metallic Pt and Pt(II) was estimated as 83.6% and 16.4%, indicating that metallic Pt was the main species. Note that, the binding energy of $Pt4f_{5/2}$ electron decreased about 0.2 eV, compared to metallic Pt (74.6 eV) in Pt/C [6,42,43]. However, for the Au4f spectra, two sharp peaks with binding energies at ~87.6 eV and ~83.8 eV can be attributed to the $Au4f_{5/2}$ and $Au4f_{7/2}$ electrons, and both binding energy values agree well with bulk gold (Au^0, ~87.6 eV and ~83.8 eV) [44–46], indicating barely binding energy shift. The decrease of the Pt4f binding energy indicated the charge transfer occurred from Au atoms to Pt atoms, which have been documented in previous reports [20,46,47]. Furthermore, the negative shift of the binding energy suggests the decrease of the d-band center of Pt, which could weaken the surface adsorption capability of poisoning intermediate, hence facilitating the reaction kinetics and significantly enhancing the catalytic activity [47].

3.3. The ORR activity comparison of the series of samples in alkaline media

The as-prepared samples were first subjected to the

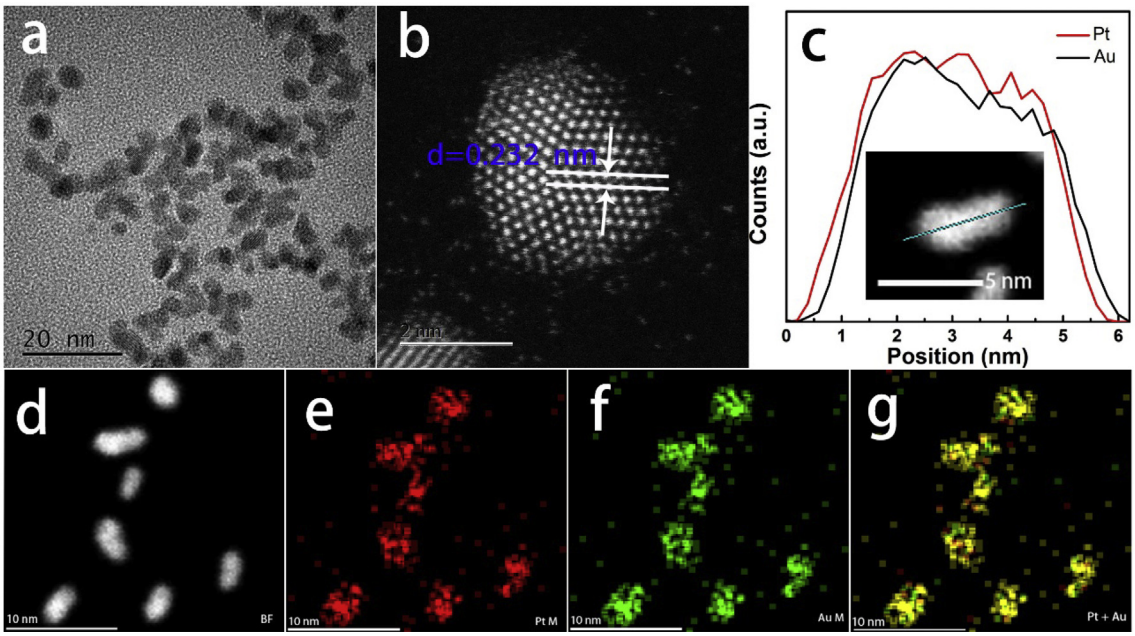

Fig. 1. (a) Representative TEM image and (b) HR-TEM image of the $Au_{33}Pt_{67}$ sample. (c) Cross-sectional compositional line-scan profiles of a single $Au_{33}Pt_{67}$ NP (inset: HAADF-STEM image). (d) Black field-TEM image of the $Au_{33}Pt_{67}$ sample and EDS elemental mapping of (e) Pt, (f) Au and (g) Pt plus Au elements in the NPs.

electrocatalytic test toward ORR. Table S1 summarizes the ORR activity results of the series of samples. The CV curves of all the samples can be found in Fig. S4a. From the RRDE voltammograms in Fig. 3a, it can be seen that, the Au_{100} sample exhibited relatively week ORR activity, besides that, all the samples demonstrated effective activity. Notably, the onset potential and diffusion-limited current density at +0.2 V varied drastically with the change of Au-to-Pt ratio among the series. As summarized in Table S1, the onset potential first increased then decreased with the decreasing of Au-to-Pt ratio, while besides the Au_{100} sample, all the samples exhibited at least comparable or more positive onset potential than Pt/C. The $Au_{33}Pt_{67}$ and $Au_{50}Pt_{50}$ samples showed the same and most positive onset potential value (1.02 V), much higher than that of Pt/C (0.98 V). Similar change trend was also observed for the diffusion-limited current density with regard to the Au-to-Pt ratio. Besides the Au_{100} sample, the diffusion-limited current density of the other samples was slightly lower than Pt/C, however, the $Au_{33}Pt_{67}$ sample exhibited the largest value (5.3 mA cm^{-2}), slightly higher than Pt/C (5.2 mA cm^{-2}). The above results indicated that the $Au_{33}Pt_{67}$ sample possessed the best activity among the series, which is further compared with Pt/C in Figs. S4b and 3b. As shown in Fig. S4b, no obvious redox peak was observed for the $Au_{33}Pt_{67}$ sample and Pt/C in N_2-saturated 0.1 M KOH solution, but a well-defined cathodic peak is clearly observed at ~0.88 V when the 0.1 M KOH solution was saturated with O_2, implying the excellent electrocatalytic activity for ORR. As depicted in Fig. 3b, the $Au_{33}Pt_{67}$ sample exhibited comparable diffusion-limited current density with Pt/C but much higher onset potential than Pt/C, suggesting higher ORR activity than Pt/C.

Furthermore, based on the RRDE data (Fig. 3b), the electron transfer number (n) and the yield of H_2O_2 in ORR can be calculated through the equations of

$$n = \frac{4I_d}{I_r/N + I_d} \quad (1)$$

$$H_2O_2\% = \frac{200I_r/N}{I_r/N + I_d} \quad (2)$$

where I_d is the disk current, I_r is the ring current, and N is the RRDE collection efficiency (0.37). The calculated results for the $Au_{33}Pt_{67}$ sample and Pt/C can be found in Fig. 3c. In the potential range of +0.2 V to +0.80 V, the electron transfer number was 3.95–3.99 and 3.96 to 3.99 for the $Au_{33}Pt_{67}$ sample and Pt/C, respectively, both values are very close to 4, indicating a 4-electron transfer pathway was adopted. Correspondingly, the H_2O_2 yield was 0.39%–2.48% and 0.39%–1.64% for the $Au_{33}Pt_{67}$ sample and Pt/C, both of them were less than 5%, suggesting negligible byproduct was produced during the catalytic process. The remarkable high electron transfer number and extremely low H_2O_2 yield indicated both of them can catalyze electroreduction of oxygen very efficiently. Moreover, the n and H_2O_2 yield of the $Au_{33}Pt_{67}$ sample was comparable with Pt/C, together with the higher onset potential, comparable diffusion-limited current density, all the findings attest that the $Au_{33}Pt_{67}$ sample possessed superior ORR activity than commercial Pt/C. Next, the reaction kinetics of the $Au_{33}Pt_{67}$ sample was disclosed and compared with Pt/C. From Figs. S4c and d, it can be observed that the voltammetric currents of the $Au_{33}Pt_{67}$ sample and Pt/C increased with the increasing of the electrode rotation rate for both samples. In addition, the corresponding Koutecky-Levich (K-L) plots of the $Au_{33}Pt_{67}$ sample and Pt/C can be found in Fig. S5. A great linearity was obtained with a quite consistent slope for both samples, implying a first reaction-kinetics with regard to the oxygen concentration in the solution. The K-L plots of the other samples in the series can be found in Fig. S6, and a good linearity was exhibited for all the samples in the potential from 0.42 V to 0.63 V.

Another method to calculate the electron transfer number is based on the K-L theory, specifically on Equation (3) [48,49], which describes the current density behavior on RDE.

$$\frac{1}{j} = \frac{1}{j_k} + \frac{1}{j_l} = \frac{1}{B\omega^{-1/2}} + \frac{1}{j_k} \quad (3)$$

where j, j_k, and j_l are the measured, kinetic-limited, and mass

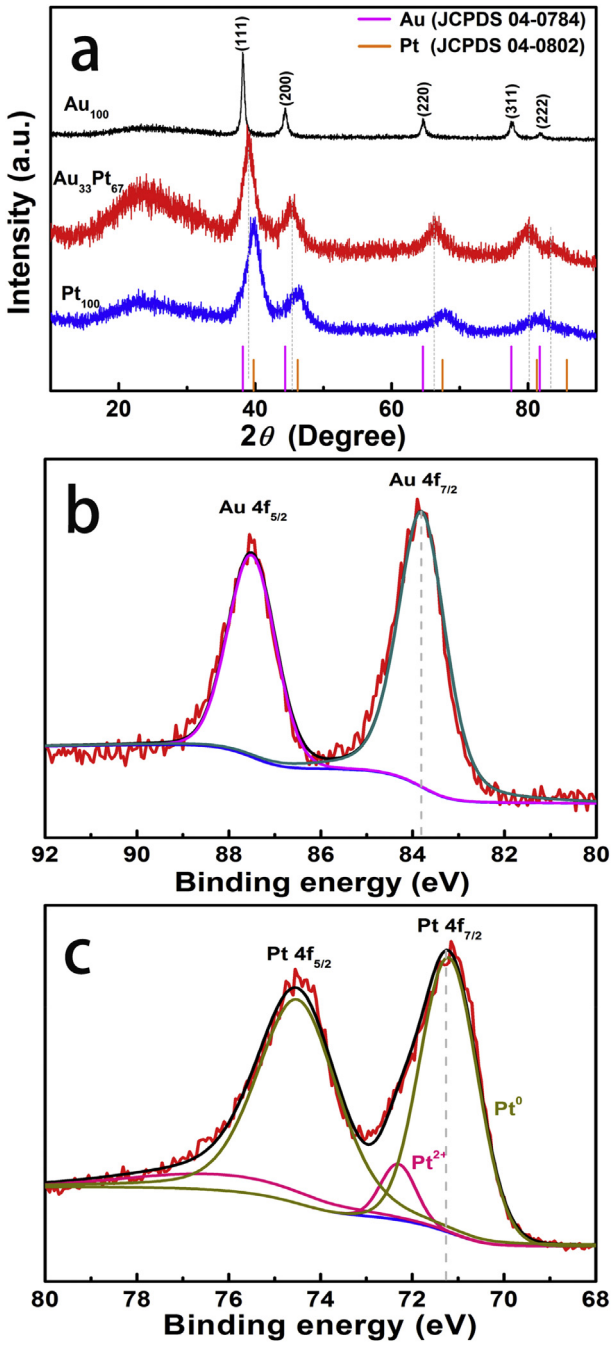

Fig. 2. (a) The XRD patterns of the $Au_{33}Pt_{67}$, Au_{100} and Pt_{100} samples, and the high-resolution XPS spectra of (b) Au4f and (c) Pt4f electrons for the $Au_{33}Pt_{67}$ sample.

transfer-limited current densities, respectively. j_k is assumed to be a constant at a certain potential, j_l is proportional to the square root of angular velocity (ω) of the RDE. The proportionality coefficient (B) is

$$B = 0.62D^{2/3}\nu^{-1/6}nFC^{*} \quad (4)$$

where n is the electron transfer number, F is the Faraday constant (96,485 C mol^{-1}), ν is the kinematic viscosity (0.01 cm^2 s^{-1}), C^{*} is the bulk concentration of O_2 (1.2×10^{-6} mol cm^{-3}), D is the diffusion coefficient of O_2 in 0.1 M KOH (1.9×10^{-5} cm^2 s^{-1}). Based on the above two equations, the electron transfer number of the $Au_{33}Pt_{67}$ sample at +0.45 V is calculated as 3.95, which is in good accordance with the n value (3.96) that obtained from RRDE measurements.

Fig. 3d displays the Tafel plots of the $Au_{33}Pt_{67}$ sample and Pt/C. It has been well documented that the Tafel slopes are typically found at 60 or 120 mV dec^{-1} for ORR, where 60 mV dec^{-1} corresponds to a pseudo-two-electron process as the rate-determining step [6,15,43] and 120 mV dec^{-1} suggests that the rate-determining step is probably a first-electron transfer to oxygen molecule, while the subsequent reduction and OO bond-breaking steps are relatively facile [50–52]. In the high overpotential range, the Tafel slope of the $Au_{33}Pt_{67}$ sample was calculated as 76.2 mV dec^{-1}, close to that of Pt/C (67.8 mV dec^{-1}), suggesting a similar reaction mechanism with Pt/C was adopted for $Au_{33}Pt_{67}$, that is, the ORR process is a pseudo-two-electron reduction step. While in the low overpotential range, the Tafel slopes of the $Au_{33}Pt_{67}$ sample and Pt/C were determined as 119.8 mV dec^{-1} and 120 mV dec^{-1}, indicating the ORR reaction rate was dominated by the first electron transfer to oxygen. [10,15,53,54]

3.4. Durability comparison of the $Au_{33}Pt_{67}$ sample and commercial Pt/C for ORR in alkaline media

The long-term durability of the $Au_{33}Pt_{67}$ sample was then evaluated and compared with Pt/C by the chronoamperometric measurements. As displayed in Fig. 4a, after continuous operation of about 2,0000 s, the cathodic current retained about 83.2% of its initial value for Pt/C, in contrast, the $Au_{33}Pt_{67}$ sample only exhibited a loss of 9.3% (90.7% retained), suggesting a much higher stability than that of commercial Pt/C. Accelerated durability test (ADT) is another important approach that can assess the long-term durability of the catalysts, and Fig. 4b and c present the ADT results of Pt/C and the $Au_{33}Pt_{67}$ sample by cycling the catalysts over the potential range from +0.2 V to +1.1 V in an O_2-saturated 0.1 M KOH solution. After 2500 cycles, the half-wave potential shifted negatively about 18 mV for Pt/C, while only 9 mV shift was observed for the $Au_{33}Pt_{67}$ sample. The results further confirmed that $Au_{33}Pt_{67}$ possessed markedly superior long-term stability than Pt/C in the electrocatalytic process of ORR in alkaline media.

3.5. The ORR activity and stability comparison of the $Au_{33}Pt_{67}$ sample with Pt/C in acid media

Moreover, the ORR activity of the $Au_{33}Pt_{67}$ sample was also evaluated and compared with Pt/C in acid electrolyte of 0.1 M $HClO_4$. Fig. 5a illustrates the polarization curves of the $Au_{33}Pt_{67}$ sample and Pt/C in O_2-saturated 0.1 M $HClO_4$ solution at a rotation rate of 1600 rpm. The onset potential of the $Au_{33}Pt_{67}$ sample was estimated as 0.98 V, which slightly higher than that of Pt/C (0.96 V). Meanwhile, the diffusion-limited current density for the $Au_{33}Pt_{67}$ sample was 5.7 mA cm^{-2}, close to that of Pt/C (6.1 mA cm^{-2}). These results suggest that the $Au_{33}Pt_{67}$ sample possessed comparable ORR activity with Pt/C in acid media. Additionally, the LSV polarization curves at different rotation rates as well as the corresponding K-L plots in 0.1 M $HClO_4$ for the $Au_{33}Pt_{67}$ sample and Pt/C can be found in Fig. S7. It can be noted that, great linearity with consistent slope was observed for the $Au_{33}Pt_{67}$ sample and Pt/C, suggesting a first reaction kinetics with respect to oxygen concentration in 0.1 M $HClO_4$ for both catalysts. The Tafel plots were then extrapolated and shown as the inset graph in Fig. 5a. The $Au_{33}Pt_{67}$ sample exhibited a Tafel slope of 75.6 mV dec^{-1}, very close to that of Pt/C, indicating the ORR also proceed with a 4-electron pathway as Pt/C. Furthermore, after continuous operation of 10,000 s, the current remained 70.2% of its initial value (Fig. 5b), about 10% higher than that of Pt/C (60.2%), suggesting a superior long-term durability than Pt/C in acid media.

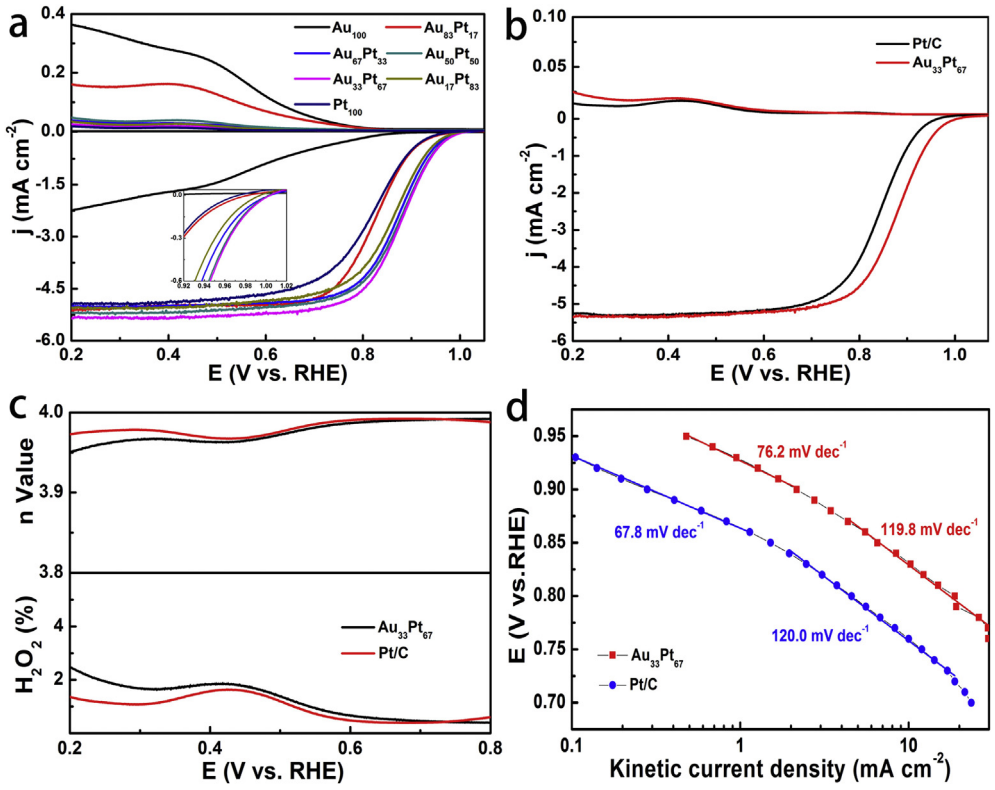

Fig. 3. (a) RRDE voltammograms of a glassy carbon electrode of the AuPt alloyed NPs in O_2-saturated 0.1 M KOH solution (inset is the amplified graph with the potential ranging from 0.92 V to 1.02 V). Potential scan rate is 10 mV s^{-1} and the rotation rate is 1600 rpm. (b) RRDE voltammograms, (c) plots of H_2O_2 yield and electron transfer numbers and (d) the corresponding Tafel plots of the $Au_{33}Pt_{67}$ sample and Pt/C catalyst.

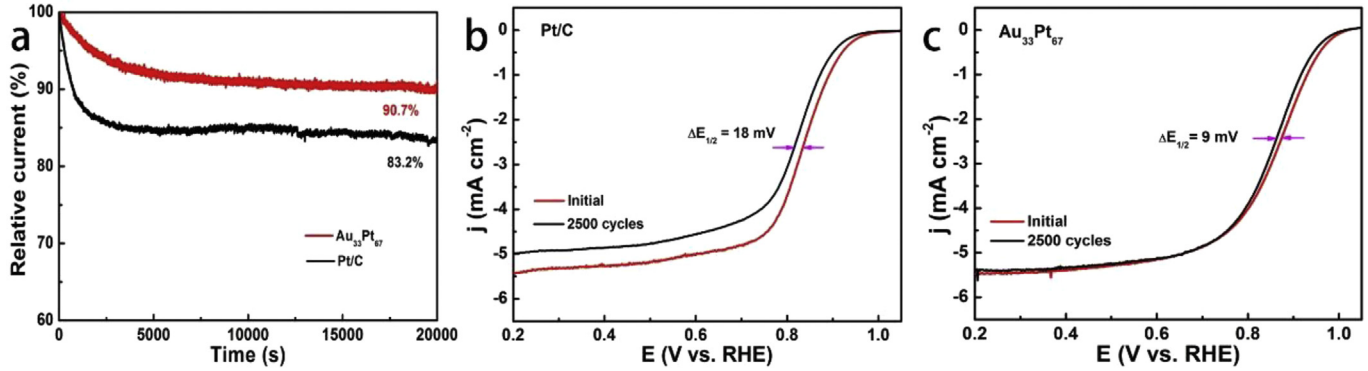

Fig. 4. (a) Chronoamperometric curves of the $Au_{33}Pt_{67}$ sample and Pt/C catalyst at +0.5 V with a rotation rate of 900 rpm for 20,000 s. The accelerated durability tests (ADT) of (b) Pt/C and (c) the $Au_{33}Pt_{67}$ sample before and after 2500 cycles from +0.6 V to 1.0 V with a rotation rate of 1600 rpm at a scan rate of 50 mV s^{-1}. All measurements were conducted in an O_2-saturated 0.1 M KOH solution.

3.6. The HER activity comparison of the series of samples with Pt/C

In addition to ORR, the electrocatalytic HER activity of the AuPt bimetallic series was also tested in comparison with Pt/C. Fig. 6a presents the polarization curves for HER in 0.1 M KOH solution. Pt/C exhibited the best HER activity, with a nearly zero onset potential. Interestingly, negligible HER activity was observed for the Au_{100} sample. Other than that, the AuPt alloys and the Pt_{100} sample displayed effective HER activity, however, the activity varied with the change of Au-to-Pt ratio. To afford a current density of 20 mA cm^{-2}, the required overpotential was −217 mV for $Au_{83}Pt_{17}$, −204 mV for $Au_{67}Pt_{33}$, −172 mV for $Au_{50}Pt_{50}$, −171 mV for $Au_{33}Pt_{67}$, −186 mV for $Au_{17}Pt_{83}$, −227 mV for Pt_{100}, and −165 mV for Pt/C, respectively. The $Au_{33}Pt_{67}$ sample displayed the best HER activity, as the smallest overpotential was observed. Such overpotential value is also close to that of Pt/C, indicating a comparable HER activity. Tafel slope is an inherent property for an electrocatalyst, and it can be obtained by fitting the linear portions of the polarization curves with the Tafel equation:

$$\eta = b \log j + a \tag{5}$$

where j is the current density and b is the Tafel slope. The Tafel slopes of the $Au_{33}Pt_{67}$ sample and Pt/C was calculated as 81 mV dec^{-1} and 73 mV dec^{-1} (Fig. 6b), further confirming that the HER activity of the $Au_{33}Pt_{67}$ sample was close to Pt/C. Then the HER

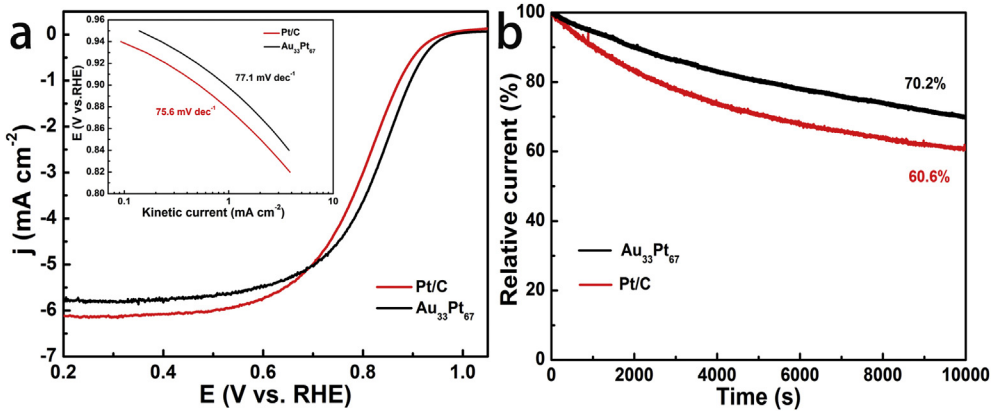

Fig. 5. (a) LSV curves and the corresponding Tafel plots (inside) of the $Au_{33}Pt_{67}$ sample and Pt/C in O_2-saturated 0.1 M $HClO_4$ solution at a rotation rate of 1600 rpm. (b) Chronoamperometric curves of the $Au_{33}Pt_{67}$ sample and Pt/C catalyst at +0.5 V for 10,000 s in 0.1 M $HClO_4$.

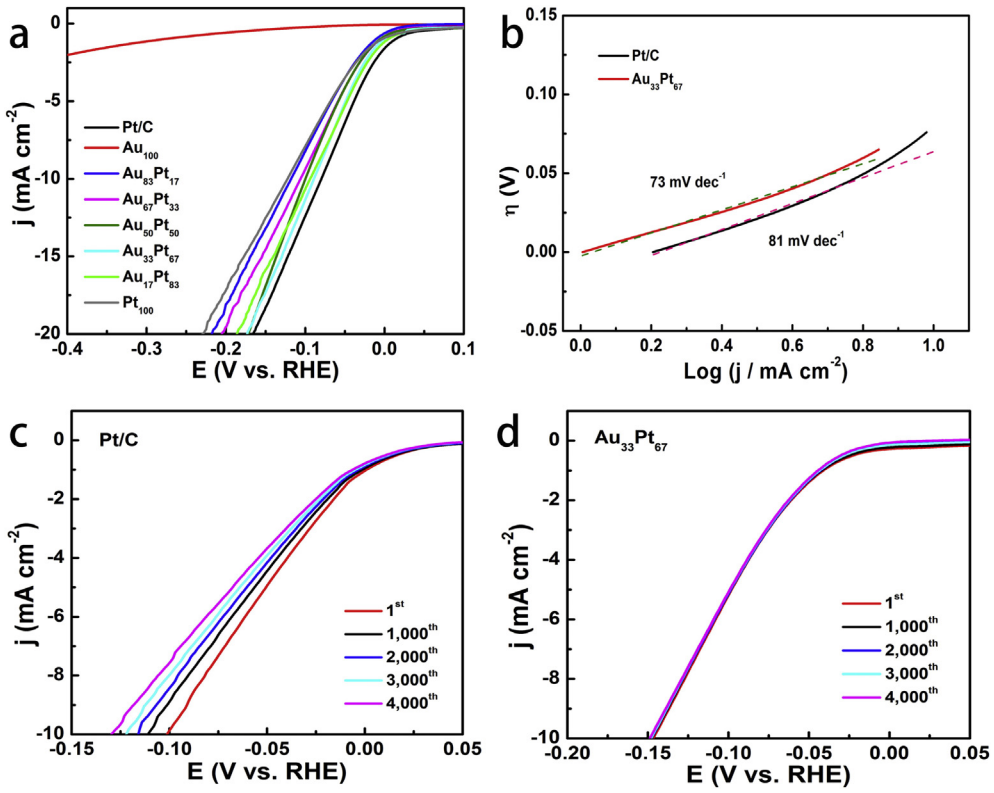

Fig. 6. (a) HER polarization curves of the AuPt alloyed NPs and Pt/C in 0.1 M KOH with scan rate of 10 mV s^{-1}. (b) The corresponding Tafel plots of the $Au_{33}Pt_{67}$ sample and Pt/C catalyst. Polarization curves after continuous potential sweeps (100 mV s^{-1}) of (c) Pt/C and (d) the $Au_{33}Pt_{67}$ sample at 10 mV s^{-1} in 0.1 M KOH.

stability of the two samples were probed and compared in alkaline electrolyte. Fig. 6c and d present the polarization curves of Pt/C and the $Au_{33}Pt_{67}$ sample before and after 4000 cycles of potential scans. By using a current density of 10 mA cm^{-2} as a metric, 29 mV potential shift was observed for Pt/C, while in contrast, after 4000 cycles, almost no potential shift can be found in the $Au_{33}Pt_{67}$ sample, suggesting a markedly superior stability in alkaline media.

Furthermore, the HER activity in acid electrolyte of 0.5 M H_2SO_4 of the AuPt alloys was also tested and the results are shown in Fig. S8. From the polarization curves in Fig. S8a, the Au_{100} sample barely exhibited HER activity, and as expected, Pt/C displayed the best activity. To afford a current density of 20 mA cm^{-2}, the required overpotential was −53 mV for $Au_{83}Pt_{17}$, −53 mV for $Au_{67}Pt_{33}$, −49 mV for $Au_{50}Pt_{50}$, −44 mV for $Au_{33}Pt_{67}$, −53 mV for $Au_{17}Pt_{83}$, −61 mV for Pt_{100}, and −33 mV for Pt/C. $Au_{33}Pt_{67}$ demonstrated the best HER activity in acidic media as well among the series. The calculated Tafel slope was 34 mV dec^{-1} for $Au_{33}Pt_{67}$ and 29 mV dec^{-1} for Pt/C (Fig. S8b), and once again confirmed that $Au_{33}Pt_{67}$ exhibited comparable HER activity with commercial Pt/C in acid electrolyte. Finally, the stability of $Au_{33}Pt_{67}$ was tested and compared with Pt/C in 0.5 M H_2SO_4. The polarization curves before and after 4000 cycles of potential scan for Pt/C and $Au_{33}Pt_{67}$ can be found in Fig. S8c and d. To afford a current density of 20 mA cm^{-2}, the required overpotential increased about 115 mV while only 19 mV potential increase was observed for $Au_{33}Pt_{67}$. The results strongly attest that $Au_{33}Pt_{67}$ possessed much higher stability than

Pt/C for HER in acid media as well.

The enhanced long-term stability for both ORR and HER of the $Au_{33}Pt_{67}$ sample is quite encouraging, and such robust stability might be attributed to the following factors: 1. The alloying effects in the product. It has been widely acknowledged that, the introduction of another metal component can tune and/or modify the surface geometric and electronic structure of the metal architectures, hence significantly improve the stability of the alloyed nanoparticles [5,8]. 2. Peptide Z1 serves as the stabilizer and capping agent, and it can prevent the strong metal-metal interaction for aggregation and/or coalescence. [35]

3.7. The ORR and HER activity comparison with other AuPt nanostructures

The remarkably excellent activity toward both ORR and HER from the $Au_{33}Pt_{67}$ sample was higher than recently reported AuPt alloys, Au@Pt core-shell structures and other AuPt bimetallic nanostructures either in alkaline or acid electrolyte. The comparison results are compiled in Table S2. For examples, in 0.1 M KOH for ORR test, the onset potential was 0.90 V, 0.96 V and 0.91 V for PtAu superlattice arrays [20], AuPt nanodendrites [24] and Pt@Au nanorods on Pyridine Graphene [55], respectively, all of them were lower than that of the $Au_{33}Pt_{67}$ sample (1.02 V). In addition, when the electrolyte was switched into 0.1 M $HClO_4$, the $Au_{33}Pt_{67}$ sample exhibited an onset potential of 0.98 V, which is also much more positive than $Au_{75}Pt_{25}$ alloyed nanodendrites (0.89 V) [56], PtAu/C-250 (0.89 V) [57], as well as Imp-PtAu/C (0.5 M $HClO_4$, 0.87 V) [58]. Furthermore, when employing 0.5 M H_2SO_4 as electrolyte for HER, to afford a current density of 10 mA cm^{-2}, the required overpotential was 30 mV for the $Au_{33}Pt_{67}$ sample, lower than that of AuPt nanostructures supported on carbon fiber (235 mV) [59] and AuPt nanodendrites (48 mV) [24], and close to that AuPdPt-WC/C (25 mV) [60]. It is worth noting that, the $Au_{33}Pt_{67}$ sample also demonstrated great capability to produce hydrogen in alkaline media, of which rare examples can be found to compare.

The remarkably high catalytic activity toward ORR and HER of the $Au_{33}Pt_{67}$ sample can be attributed to the Au–Pt alloying induced synergistic effects, namely the geometric effects and the electronic effects. The combination of two metals can lead to formation of hetero-atom bond, hence resulting in generation of new catalytic active sites [2,4], and this is so called geometric effect. Meanwhile, the introduction of Au atoms to Pt nanoparticles (versa vice) can largely alter and modify the electronic structure of the metal nanoparticles, evidenced by the electron transfer phenomenon observed in XPS measurement for the $Au_{33}Pt_{67}$ sample. Such electronic effect can be crucial for the enhancement of the electrocatalytic activity. Take ORR as an example, Pt has strong binding affinity to oxygenated intermediates, while the introduction of a relatively weak binder (Au) can “dilute” the strong interaction at the atomic level. The weakened binding interaction led to the enhanced activity with a maximum of the $Au_{33}Pt_{67}$ sample. Moreover, further increase of the Au content or the Pt content can result in the interaction either too strong or too weak, both of which would diminish the ORR activity. The maximum activity of $Au_{33}Pt_{67}$ sample represents the optimal balance. Such perfect alloying effects can be further evidenced by the HAADF-STEM images with homogeneously well-mixed Pt–Au patterns and well-maintained Pt crystalline. As a note, previous studies have shown that the bimetallic AuPt synergistic effects can significantly promote the electrokinetics of ORR and HER. [19,20,23,24]

4. Conclusions

In summary, a series of bimetallic AuPt alloyed nanoparticles were fabricated by employing Z1 as template/ligand. $Au_{33}Pt_{67}$ exhibited well-defined peanut shape, while spherical particles were obtained for the other samples in the series. The series of AuPt bimetallic nanoparticles demonstrated effective electrocatalytic activities toward both ORR and HER. $Au_{33}Pt_{67}$ exhibited the best bifunctional catalytic activities among the series, of which the ORR activity was superior than commercial Pt/C while the HER activity is close to Pt/C in alkaline media. Such remarkable bifunctional electrocatalytic activities are ascribed to the Au alloying Pt induced synergistic effects. Moreover, $Au_{33}Pt_{67}$ demonstrated markedly higher long-term stability than Pt/C in both ORR and HER. The findings can shed light upon further rational design and engineering of peptide templated bimetallic nanomaterials with premium activity and robust stability for dual or even multiple electrocatalytic reactions.

Acknowledgements

This work was supported by the National Natural Science Foundation of China (No. 21501059). Z.H.T also acknowledges financial support from Project of Public Interest Research and Capacity Building of Guangdong Province (No. 2015A010105009), Guangdong Innovative and Entrepreneurial Research Team Program (No. 2014ZT05N200), and Guangdong Natural Science Funds for Distinguished Young Scholars (No. 2015A030306006).

Appendix A. Supplementary data

Supplementary data related to this article can be found at https://doi.org/10.1016/j.electacta.2017.11.057.

References

[1] H.-L. Jiang, Q. Xu, Recent progress in synergistic catalysis over heterometallic nanoparticles, J. Mater. Chem. 21 (2011) 13705–13725.
[2] K.D. Gilroy, A. Ruditskiy, H.-C. Peng, D. Qin, Y. Xia, Bimetallic nanocrystals: syntheses, properties and applications, Chem. Rev. 116 (2016) 10414–10472.
[3] F. Tao, Synthesis, catalysis, surface chemistry and structure of bimetallic nanocatalysts, Chem. Soc. Rev. 41 (2012) 7977–7979.
[4] I. Notar Francesco, F. Fontaine-Vive, S. Antoniotti, Synergy in the catalytic activity of bimetallic nanoparticles and new synthetic methods for the preparation of fine chemicals, ChemCatChem 6 (2014) 2784–2791.
[5] C. Wang, N.M. Markovic, V.R. Stamenkovic, Advanced platinum alloy electrocatalysts for the oxygen reduction reaction, ACS Catal. 2 (2012) 891–898.
[6] L. Wang, Z. Tang, W. Yan, Q. Wang, H. Yang, S. Chen, Co@Pt Core@Shell nanoparticles encapsulated in porous carbon derived from zeolitic imidazolate framework 67 for oxygen electroreduction in alkaline media, J. Power Sources 343 (2017) 458–466.
[7] X. Huang, Z. Zhao, L. Cao, Y. Chen, E. Zhu, Z. Lin, M. Li, A. Yan, A. Zettl, Y.M. Wang, X. Duan, T. Mueller, Y. Huang, High-performance transition metal–doped Pt_3Ni octahedra for oxygen reduction reaction, Science 348 (2015) 1230–1234.
[8] W. Wang, B. Lei, S. Guo, Engineering multimetallic nanocrystals for highly efficient oxygen reduction catalysts, Adv. Energy Mater. 6 (2016), 1600236.
[9] G. Wu, A. Santandreu, W. Kellogg, S. Gupta, O. Ogoke, H. Zhang, H.-L. Wang, L. Dai, Carbon nanocomposite catalysts for oxygen reduction and evolution reactions: from nitrogen doping to transition-metal addition, Nano Energy 29 (2016) 83–110.
[10] M. Liu, R. Zhang, W. Chen, Graphene-supported nanoelectrocatalysts for fuel cells: synthesis, properties and applications, Chem. Rev. 114 (2014) 5117–5160.
[11] L. Zhang, Q. Chang, H. Chen, M. Shao, Recent advances in palladium-based electrocatalysts for fuel cell reactions and hydrogen evolution reaction, Nano Energy 29 (2016) 198–219.
[12] J. Wang, F. Xu, H. Jin, Y. Chen, Y. Wang, Non-noble metal-based carbon composites in hydrogen evolution reaction: fundamentals to applications, Adv. Mater. 29 (2017), 1605838.
[13] W. Chen, S. Chen, Oxygen electroreduction catalyzed by gold nanoclusters: strong core size effects, Angew. Chem. Int. Ed. 48 (2009) 4386–4389.
[14] Q. Wang, L. Wang, Z. Tang, F. Wang, W. Yan, H. Yang, W. Zhou, L. Li, X. Kang, S. Chen, Oxygen reduction catalyzed by gold nanoclusters supported on carbon nanosheets, Nanoscale 8 (2016) 6629–6635.
[15] L. Wang, Z. Tang, W. Yan, H. Yang, Q. Wang, S. Chen, Porous carbon-supported gold nanoparticles for oxygen reduction reaction: effects of nanoparticle size, ACS Appl. Mater. Interfaces 8 (2016) 20635–20641.

[16] J. Luo, P.N. Njoki, Y. Lin, L. Wang, C.J. Zhong, Activity-composition correlation of AuPt alloy nanoparticle catalysts in electrocatalytic reduction of oxygen, Electrochem. Commun. 8 (2006) 581–587.
[17] Y. Kim, J.W. Hong, Y.W. Lee, M. Kim, D. Kim, W.S. Yun, S.W. Han, Synthesis of AuPt heteronanostructures with enhanced electrocatalytic activity toward oxygen reduction, Angew. Chem. Int. Ed. 49 (2010) 10197–10201.
[18] P. Song, S.-S. Li, L.-L. He, J.-J. Feng, L. Wu, S.-X. Zhong, A.-J. Wang, Facile large-scale synthesis of Au-Pt alloyed nanowire networks as efficient electrocatalysts for methanol oxidation and oxygen reduction reactions, RSC Adv. 5 (2015) 87061–87068.
[19] L.-L. He, P. Song, A.-J. Wang, J.-N. Zheng, L.-P. Mei, J.-J. Feng, A general strategy for the facile synthesis of AuM (M = Pt/Pd) alloyed flowerlike-assembly nanochains for enhanced oxygen reduction reaction, J. Mater. Chem. A 3 (2015) 5352–5359.
[20] J.-J. Feng, L.-L. He, R. Fang, Q.-L. Wang, J. Yuan, A.-J. Wang, Bimetallic PtAu superlattice arrays: highly electroactive and durable catalyst for oxygen reduction and methanol oxidation reactions, J. Power Sources 330 (2016) 140–148.
[21] L. Sun, H. Wang, K. Eid, L. Wang, Shape-controlled synthesis of porous AuPt nanoparticles and their superior electrocatalytic activity for oxygen reduction reaction, Sci. Technol. Adv. Mater. 17 (2016) 58–62.
[22] F.-Q. Shao, X.-X. Lin, J.-J. Feng, J. Yuan, J.-R. Chen, A.-J. Wang, Simple fabrication of core-shell AuPt@Pt nanocrystals supported on reduced graphene oxide for ethylene glycol oxidation and hydrogen evolution reactions, Electrochim. Acta 219 (2016) 321–329.
[23] J.-J. Feng, L.-X. Chen, X. Ma, J. Yuan, J.-R. Chen, A.-J. Wang, Q.-Q. Xu, Bimetallic AuPt alloy nanodendrites/reduced graphene oxide: one-pot ionic liquid-assisted synthesis and excellent electrocatalysis towards hydrogen evolution and methanol oxidation reactions, Int. J. Hydrogen Energy 42 (2017) 1120–1129.
[24] J.-J. Feng, L. Liu, X. Ma, J. Yuan, A.-J. Wang, Ultrasonication-assisted wet-chemical fabrication of uniform AuPt nanodendrites as efficient electrocatalyst for oxygen reduction and hydrogen evolution reactions, Int. J. Hydrogen Energy 42 (2017) 2071–2080.
[25] L. Luo, Z. Duan, H. Li, J. Kim, G. Henkelman, R.M. Crooks, Tunability of the adsorbate binding on bimetallic alloy nanoparticles for the optimization of catalytic hydrogenation, J. Am. Chem. Soc. 139 (2017) 5538–5546.
[26] M.B. Dickerson, K.H. Sandhage, R.R. Naik, Protein- and peptide-directed syntheses of inorganic materials, Chem. Rev. 108 (2008) 4935–4978.
[27] M.R. Jones, K.D. Osberg, R.J. Macfarlane, M.R. Langille, C.A. Mirkin, Templated techniques for the synthesis and assembly of plasmonic nanostructures, Chem. Rev. 111 (2011) 3736–3827.
[28] B.D. Briggs, M.R. Knecht, Nanotechnology meets biology: peptide-based methods for the fabrication of functional materials, J. Phys. Chem. Lett. 3 (2012) 405–418.
[29] R. Bhandari, R. Coppage, M.R. Knecht, Mimicking Nature's strategies for the design of nanocatalysts, Catal. Sci. Technol. 2 (2012) 256–266.
[30] J.P. Palafox-Hernandez, Z. Tang, Z.E. Hughes, Y. Li, M.T. Swihart, P.N. Prasad, T.R. Walsh, M.R. Knecht, Comparative study of materials-binding peptide interactions with gold and silver surfaces and nanostructures: a thermodynamic basis for biological selectivity of inorganic materials, Chem. Mater. 26 (2014) 4960–4969.
[31] N.M. Bedford, A.R. Showalter, T.J. Woehl, Z.E. Hughes, S. Lee, B. Reinhart, S.P. Ertem, E.B. Coughlin, Y. Ren, T.R. Walsh, B.A. Bunker, Peptide-directed PdAu nanoscale surface segregation: toward controlled bimetallic architecture for catalytic materials, ACS Nano 10 (2016) 8645–8659.
[32] Y.-S. Ko, Y.-T. Kim, J.-H. Kim, D.H. Kim, K.-H. Kim, W.S. Yun, Y.D. Kim, J. Lee, Y.H. Kim, Peptide-based bimetallic nanostructures with tailored surface compositions and their oxygen electroreduction activities, CrystEngComm 18 (2016) 6024–6028.
[33] Q. Wang, H. Yang, Z. Zhou, L. Wang, W. Yan, W. Wu, S. Chen, Z. Liu, Z. Tang, Peptide A4 based AuAg alloyed nanoparticle networks for electrocatalytic reduction of oxygen, Int. J. Hydrogen Energy 42 (2017) 11295–11303.
[34] D. Li, Z. Tang, S. Chen, Y. Tian, X. Wang, Peptide-FlgA3-Based gold palladium bimetallic nanoparticles that catalyze the oxygen reduction reaction in alkaline solution, ChemCatChem 9 (2017) 2980–2987.
[35] B.R. Peelle, E.M. Krauland, K.D. Wittrup, A.M. Belcher, Design criteria for engineering inorganic material-specific peptides, Langmuir 21 (2005) 6929–6933.
[36] Z. Tang, J.P. Palafox-Hernandez, W.-C. Law, Z.E. Hughes, M.T. Swihart, P.N. Prasad, M.R. Knecht, T.R. Walsh, Biomolecular recognition principles for bionanocombinatorics: an integrated approach to elucidate enthalpic and entropic factors, ACS Nano 7 (2013) 9632–9646.
[37] Y. Li, Z. Tang, P.N. Prasad, M.R. Knecht, M.T. Swihart, Peptide-mediated synthesis of gold nanoparticles: effects of peptide sequence and nature of binding on physicochemical properties, Nanoscale 6 (2014) 3165–3172.
[38] Q. Wang, Z. Tang, L. Wang, H. Yang, W. Yan, S. Chen, Morphology control and electro catalytic activity towards oxygen reduction of peptide-templated metal nanomaterials: a comparison between Au and Pt, Chem. Sel. 1 (2016) 6044–6052.
[39] R. Bhandari, M.R. Knecht, Synthesis, characterization, and catalytic application of networked Au nanostructures fabricated using peptide templates, Catal. Sci. Technol. 2 (2012) 1360–1366.
[40] N.A. Merrill, T.T. Nitka, E.M. McKee, K.C. Merino, L.F. Drummy, S. Lee, B. Reinhart, Y. Ren, C.J. Munro, S. Pylypenko, A.I. Frenkel, N.M. Bedford, M.R. Knecht, Effects of metal composition and ratio on peptide-templated multimetallic PdPt nanomaterials, ACS Appl. Mater. Interfaces 9 (2017) 8030–8040.
[41] J.A. Creighton, D.G. Eadon, Ultraviolet-visible absorption spectra of the colloidal metallic elements, J. Chem. Soc. Faraday Trans. 87 (1991) 3881–3891.
[42] C.D. Wagner, W.M. Riggs, L.E. Davis, J.F. Moudler, G.E. Muilenberg, Handbook of X-ray Photoelectron Spectroscopy: a Reference Book of Standard Data for Use in X-ray Photoelectron Spectroscopy, Perkin-Elmer Corp., Edern Prairie, MN, 1979, p. 1979.
[43] G. He, Y. Song, K. Liu, A. Walter, S. Chen, S. Chen, Oxygen reduction catalyzed by platinum nanoparticles supported on graphene quantum dots, ACS Catal. 3 (2013) 831–838.
[44] Z. Tang, B. Xu, B. Wu, M.W. Germann, G. Wang, Synthesis and structural determination of multidentate 2,3-dithiol-stabilized Au clusters, J. Am. Chem. Soc. 132 (2010) 3367–3374.
[45] P. Zhang, X-ray spectroscopy of gold–thiolate nanoclusters, J. Phys. Chem. C 118 (2014) 25291–25299.
[46] Y.-C. Shi, J.-J. Feng, S.-S. Chen, G.-M. Tu, J.-R. Chen, A.-J. Wang, Simple synthesis of hierarchical AuPt alloy nanochains for construction of highly sensitive hydrazine and nitrite sensors, Mater. Sci. Eng. C 75 (2017) 1317–1325.
[47] C. Du, X. Gao, Z. Zhuang, C. Cheng, F. Zheng, X. Li, W. Chen, Epitaxial growth of zigzag PtAu alloy surface on Au nano-pentagrams with enhanced Pt utilization and electrocatalytic performance toward ethanol oxidation reaction, Electrochim. Acta 238 (2017) 263–268.
[48] R. Zhou, Y. Zheng, M. Jaroniec, S.-Z. Qiao, Determination of the electron transfer number for the oxygen reduction reaction: from theory to experiment, ACS Catal. 6 (2016) 4720–4728.
[49] Y. Zhang, H. Liu, H. Wu, Z. Sun, L. Qian, Facile synthesis of Pt nanoparticles loaded porous graphene towards oxygen reduction reaction, Mater. Des. 96 (2016) 323–328.
[50] X. Liu, L. Li, W. Zhou, Y. Zhou, W. Niu, S. Chen, High-performance electrocatalysts for oxygen reduction based on nitrogen-doped porous carbon from hydrothermal treatment of glucose and dicyandiamide, ChemElectroChem 2 (2015) 803–810.
[51] S. Chen, Z. Wei, X. Qi, L. Dong, Y.-G. Guo, L. Wan, Z. Shao, L. Li, Nanostructured polyaniline-decorated Pt/C@PANI core–shell catalyst with enhanced durability and activity, J. Am. Chem. Soc. 134 (2012) 13252–13255.
[52] R. Li, Z. Wei, X. Gou, Nitrogen and phosphorus dual-doped graphene/carbon nanosheets as bifunctional electrocatalysts for oxygen reduction and evolution, ACS Catal. 5 (2015) 4133–4142.
[53] C.-H. Cui, S.-H. Yu, Engineering interface and surface of noble metal nanoparticle nanotubes toward enhanced catalytic activity for fuel cell applications, Acc. Chem. Res. 46 (2013) 1427–1437.
[54] Y. Jiao, Y. Zheng, M. Jaroniec, S.Z. Qiao, Design of electrocatalysts for oxygen- and hydrogen-involving energy conversion reactions, Chem. Soc. Rev. 44 (2015) 2060–2086.
[55] X. Zhong, H. Yu, X. Wang, L. Liu, Y. Jiang, L. Wang, G. Zhuang, Y. Chu, X. Li, J.-g. Wang, Pt@Au nanorods uniformly decorated on pyridyne cycloaddition graphene as a highly effective electrocatalyst for oxygen reduction, ACS Appl. Mater. Interfaces 6 (2014) 13448–13454.
[56] P. Song, L. Liu, J.-J. Feng, J. Yuan, A.-J. Wang, Q.-Q. Xu, Poly(ionic liquid) assisted synthesis of hierarchical gold-platinum alloy nanodendrites with high electrocatalytic properties for ethylene glycol oxidation and oxygen reduction reactions, Int. J. Hydrogen Energy 41 (2016) 14058–14067.
[57] Y. Zhang, Q. Huang, Z. Zou, J. Yang, W. Vogel, H. Yang, Enhanced durability of Au cluster decorated Pt nanoparticles for the oxygen reduction reaction, J. Phys. Chem. C 114 (2010) 6860–6868.
[58] P. Hernández-Fernández, S. Rojas, P. Ocón, J.L. Gómez de la Fuente, J. San Fabián, J. Sanza, M.A. Peña, F.J. García-García, P. Terreros, J.L.G. Fierro, Influence of the preparation route of bimetallic Pt–Au nanoparticle electrocatalysts for the oxygen reduction reaction, J. Phys. Chem. C 111 (2007) 2913–2923.
[59] B. Zhang, H. Zhu, M. Zou, X. Liu, H. Yang, M. Zhang, W. Wu, J. Yao, M. Du, Design and fabrication of size-controlled Pt–Au bimetallic alloy nanostructure in carbon nanofibers: a bifunctional material for biosensors and the hydrogen evolution reaction, J. Mater. Sci. 52 (2017) 8207–8218.
[60] M. Nie, X. Liu, B. He, Q. Li, S. Du, S. Lu, C. Jiang, D. Lei, Investigation of the AuPdPt-WC/C electrocatalyst for hydrogen evolution reaction, J. Electrochem. Soc. 163 (2016) H485–H490.